COUPLED CHEMICAL AND RADIATION HYDRODYNAMICAL MODELING OF HOT CORINOS: FORMATION AND PROCESSING OF ICES

Author: Brielle Shope
Advisor: Robin T. Garrod
University of Virginia

Abstract: We present a coupled multidimensional radiation hydrodynamic and chemical model of a hot corino, tracing the evolution of ice chemistry from the pre-stellar collapse through disk formation and capturing the spatial distribution of simple species and COMs through these stages. Calculated ice column densities are compared to JWST and Spitzer data for all three YSO stages (Classes -I, 0, and I). We examine the effect of viewing angle on column density and find that the most variation occurs for inclinations between 60 and 90 degrees (edge-on). Our current chemical model underproduces carbon-bearing ice species, indicating there may be a higher abundance of carbon-bearing molecules on the grains than we currently simulate. The model also reveals the effect of meridonial circulation in the disk structure and the movement of material - some of which experiences hot core-like behavior leading to low abundances of some species on the grain surface. We find pathways for trajectories that are able to survive the harsh environment of the protostar, giving insight to the potential species preservation that might be incorporated into comets. These results have direct implications for understanding the molecular origins of the early solar system and interpreting future observational studies of protostellar chemistry.

Introduction

Recent findings indicate that many complex -- and potentially pre-biotic -- molecules present in the young solar system may have their origins in the very earliest stages of star formation (Drozdovskaya et al., 2019). Observations of low-mass star-forming cores called “hot corinos” may therefore provide us with insight into the chemical conditions that were present when the young Sun was forming, prior to the formation of the protoplanetary disk (the Class II Young Stellar Object or YSO stage) that eventually yielded planets and comets. Hot corinos, associated with YSOs of Class 0-I, are particularly noteworthy due to the great diversity and complexity of gas-phase organic molecules that are detected there, through microwave molecular emission spectroscopy using instruments such as the Atacama Large Millimeter Array (ALMA). The largest complex organic molecules (COMs) detected in hot corinos include species such as methanol CH_3OH and glycolaldehyde ($HCOCH_2OH$) (Jørgensen et al., 2012); the most complex species detected in hot, star-forming sources are usually detected in hot cores, the high-mass equivalents of hot corinos, and include propanol (C_3H_7OH) (Belloche et al., 2022; Jiménez-Serra et al., 2022) and urea (NH_2CONH_2) (Belloche et al., 2019).

The origins of many COMs are understood to involve chemistry occurring on dust grain-surfaces when the core is still relatively cold (~10 K), producing ices that later desorb during the ``hot'' stage (T $\gtrsim$ 100 K), when the protostar warms the surrounding dust and gas (Herbst & van Dishoeck, 2009). ALMA has provided much evidence concerning COMs in the hot regions (Jørgensen et al., 2020), and now data coming from James Webb Space Telescope (JWST) projects such as CORINOS (Yang et al., 2022), the Early Science Project IceAge (McClure et al., 2023; Rocha et al., 2025), and JOYS+ (Rocha et al., 2024) are providing further information about the presence and spatial distribution of solid-phase COMs in solar-type systems.

Much evidence now points to many COMs being present in the very first stages of star formation, during the pre-stellar stage before a protostar is even formed (Megías et al., 2022; Bacmann et al., 2012, Marcelino et al., 2007, Öberg et al., 2010; Jiménez-Serra et al., 2016), when dust and gas temperatures are $\lesssim$10 K. Laboratory experimental data indicate that COM production at such temperatures can be efficient on ice surfaces in tandem with the chemical production of simpler, more abundant ice species such as formaldehyde and methanol, through the repetitive hydrogenation of CO (Fedoseev et al. 2015, 2017; Chuang et al., 2016). Chemical kinetics models similarly show efficient low-temperature COM production, with non-diffusive chemistry playing the key role in reproducing the observed abundances of molecules

in star-forming regions (Jin & Garrod 2020, Garrod et al., 2022, Ioppolo et al., 2020). However, further chemistry -- both on grains and in the gas phase -- is expected to occur after the protostar has formed within its surrounding envelope (Class 0) and as the envelope accretes substantially onto the protostar and nascent disk (Class I).

The viewing angle of a source is also expected to have an effect on the observed column densities. There has been discussion as to whether the viewing angle of the observer to the disk (edge on, face-on, or somewhere in between) would affect whether a source is observed to be COM-rich or COM-poor (Nazari et al., 2022). When viewed edge-on, the mm-wavelength emission used to determine the column density of a molecule must comprise contributions from material under a range of conditions radially through the disk and envelope. However, the dust itself may make a substantial contribution to the opacity, leading to the obscuration of the molecular emission.

To determine from a modeling perspective the nature, distribution and origins of COMs and their emission in hot corinos, it is necessary to have: (i) astrochemical models that are capable of simulating COM chemical kinetics both on the dust grains and in the gas; (ii) realistic physical/dynamical models to combine with the chemical models, so that the motions of gas and dust, beginning in the pre-stellar stage and culminating in the formation of a disk, can be properly coupled to the chemical evolution; and (iii) the ability to simulate the coupled molecular and dust radiative transfer that leads to molecular line spectra that can be converted into estimates of column density as they would be measured in real observations. Only then can a full spatial picture of COM chemistry be built up.

Here we present calculations using advanced chemo-dynamical models that include explicit RHD treatments of the Class 0 – I stages, and a semi-empirical treatment for the formation of the preceding prestellar core. A detailed chemical treatment of both gas-phase and grain-surface ice and COM production is coupled with the outputs of the dynamical models. This approach will be necessary to properly interpret current and future JWST and ALMA observations and to test hypotheses on the origins of COMs in hot corinos.

We use the astrochemical model MAGICKAL (Model for Astrophysical Gas and Ice Chemical Kinetics and Layering), which is a three-phase chemical kinetics model (gas, grain-surface, and mantle-ice chemistry (Garrod, 2013). This model has many capabilities including the ability to trace ice and gas abundances of Young Stellar Objects (YSOs) from Class 0 through I. The model has perhaps the most advanced network for COMs, and is unique in having a full, self-consistent framework for the treatment of both diffusive and non-diffusive grain-surface and bulk-ice chemical reactions, using the framework set up by Jin & Garrod (2020) and Garrod et al. (2022). Coupled with a multidimensional hydrodynamics model that provides time-dependent gas-density and dust-temperature distributions under solar-type conditions, it creates a self-consistent chemical and physical picture of COM chemistry during the early stages of Solar System formation.

The present paper focuses on the ice column densities over time and their distribution throughout the disk as time evolves. A follow-up paper will focus on the analysis of the simulated gas-phase molecular data. Both ice and gas data will be compared to ALMA and JWST observations. For this paper, the models are compared with existing JWST ice data and other sources found in literature. These include JWST observations by McClure et al. (2023), Rocha et al. (2024), and Rocha et al. (2025) as well as the reported observational values in Boogert et al. (2015).

Methods

Two main computational codes are used to carry out the simulations: *ATHENA++* for the radiation hydrodynamics (RHD) and *MAGICKAL* for the chemistry, with the latter run in post-processing, based on physical conditions determined from Lagrangian tracer particles. In this main section we present an overview of the basic modeling approach. Greater detail on the entire modeling framework can be found in Bonfand et al. (in prep.).

The 2D axisymmetric RHD model simulates the evolving density, temperature, and velocity structure of the gas leading to the formation of a YSO, beginning from a singular isothermal sphere with power-law density distribution representing a prestellar core, and ending with a structure representing a protostar, circumstellar disk, and envelope. A semi-empirical model is used (see Lam, 2022, and Bonfand et al. 2025) to determine the physical/dynamical evolution of the object prior

to the initial conditions of the RHD simulation, beginning from a uniform, cold, spherical cloud and ending with the power-law density distribution. In this treatment, the initial cloud is treated as a set of spherical shells, with each initially moving at nearly constant velocity; toward the end of this condensation stage, the velocity gradually decreases to smoothly match the initial conditions of the accretion phase.

Lagrangian tracer particles calculated in post-processing are used consistently across the two stages of dynamical evolution, so that the chemistry can be systematically simulated throughout. The time-dependent gas density, temperature, and radial visual extinction values for each tracer are fed to the chemical model. The chemical simulations for each tracer are then run independently from each other, in two stages corresponding to the initial condensation from a uniform cloud (which we label stage 1) and the RHD simulation (stage 2).

This coupled dynamical/chemical treatment is essentially the same as that employed by Bonfand et al. (in prep.), but using a lower total mass in the simulations, and with a more complex system of assigning tracer particles.

Stage 1 of the model is identified with the formation of a prestellar core, sometimes referred to as Class -I. Stage 2 of the model is identified with the evolution of the prestellar core into a Class 0 source, and then into Class I. In the analysis of our model, we designate the moment when the protostellar mass first exceeds half of the total mass in the simulation as being the threshold between the Class 0 and I stages. The RHD model is stopped when the disk reaches a radius of ~300 AU, which is achieved at time 220,000 yr.

Lagrangian tracer-particle trajectories are calculated in post-processing, and the resultant time-dependent physical conditions are fed to the chemical models to calculate the stage-1 and stage-2 evolution. In stage 2, the chemistry for each tracer particle is calculated throughout the simulation time or until it enters the inner boundary representing the protostar. Careful selection of the tracers is required to ensure good spatial coverage for the chemistry at any particular moment. A total of 12 evenly spaced ``snapshot times" are chosen, and tracer particles selected, such that the instantaneous distribution of tracers provides good spatial coverage of the chemical results at those times.

Results

Hydrodynamical Data

An important part in understanding the results of the subsequent chemical modeling of each trajectory is first evaluating how the hydrodynamical model is behaving. Figure 1 shows the gas density distribution of the RHD model in the inner 300 AU of the simulation for twelve snapshot times in stage 2. The first six snapshots, from t = 0 yrs to t = 120,000 yrs, correspond to a class 0 YSO. At the eighth snapshot, the mass of the surrounding envelope is less than the protostar mass, which then classifies it as the first snapshot for a class I YSO. At the snapshot time of 120,000 yrs, a disk starts to form as demonstrated by the sudden jump in density around the midplane.

A physical feature of the hydrodynamical setup is the effect of the density profile and disk velocity field on the pathways of the trajectories. As the disk starts to form around t = 120,000 yr, the trajectories that accrete onto the disk will, in general, continue to travel outwards with the growing disk. Most trajectories are pulled toward the protostar and if their velocity is such that they join the disk, we have found that the trajectories are traveling outward along the midplane, likely as a result of angular momentum redistribution inside the disk, with the midplane material gaining angular momentum and thus expanding outward. The midplane expanding gas is stopped near the (radial) outer edge of the disk by the envelope infall, where it is forced to move upward (away from the midplane) before circulating back toward the central protostar, forming large meridional vortices that were also present in Tu et al. (2022) and Asmita et al. (2024); the latter authors considered the flow pattern a form of ``turbulence." This effect occurs within the disk and also occurs on the outer edge of the disk.

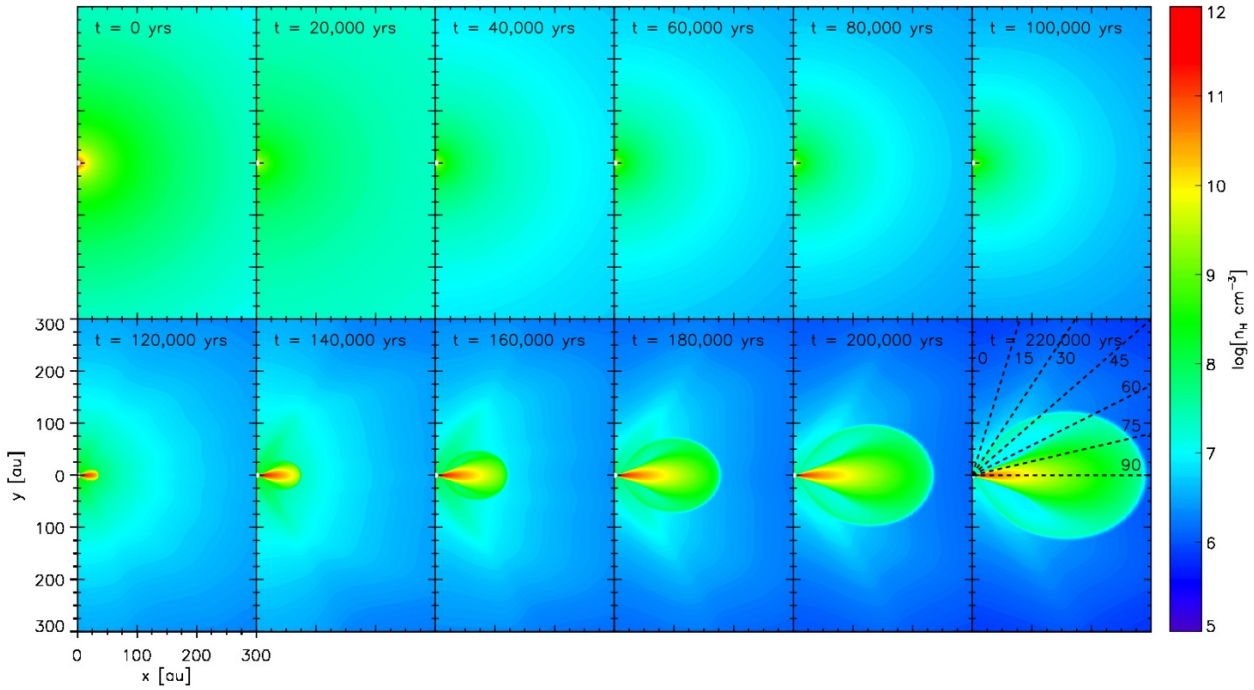

Figure 1. The density distribution over the twelve snapshot times. The last panel includes an overlay of selected inclinations, or viewing angles, into the disk, ranging from 0 (face-on) to 90 (edge-on) degrees.

Protostellar Ice Abundance Maps

Whereas in the pre-stellar collapse phase where there is only radial variation in abundance, the protostellar phase involves a two-dimensional spatial dependence due to the formation of a disk. In general, as the disk structure begins to form, the density increases towards the midplane (see Figure 1) and the temperature will decrease along the midplane. Temperatures are highest nearest the protostar and reach values as high as 729~K.

During the protostellar phase, there are various hydrodynamical processes in place that affect the pathways of trajectories. In Figure 3 the top panel shows the chemical abundance of CO for the last six snapshot times, representing the formation of a disk. This plot shows the paths of two representative trajectories that result in different chemical abundances due to physical effects. Each trajectory's path is indicated by the line that follows behind. The solid-line trajectory path is pulled towards the protostar as it falls inward with other accreting material. Instead of falling into the protostar, it is pushed along the midplane of the disk until it ends up near the middle of the disk, with a ``normal'' abundance.

However, the dashed-line trajectory experiences a different path and subsequently, a lower abundance. This trajectory gets closer to the protostar than the solid-line trajectory. This path closer to the protostar makes this trajectory subject to higher temperatures. The dashed-line trajectory experiences a temperature of 164K nearest the protostar, which is higher than the temperature required to desorb water in our model (120K). In contrast, the solid-line trajectory only reaches a temperature of 116 K. Once water is desorbed from the grain surface for the dashed-line trajectory, other grain species will rise to the surface and desorb. Each species will desorb depending on the temperature required to desorb them from the surface. The dashed-line trajectory reaches a temperature high enough to desorb CO from the grain surface and results in a lower CO abundance on the grain.

After the close approach to the protostar, the dashed-line trajectory is then pushed out along the midplane. This trajectory is then subject to meridonial circulation, in which it is pushed out of the midplane and then recycled back into the midplane of the disk. The trajectory continues along the midplane but is then pushed out at the edge of the disk due to the external pressure due to the sharp

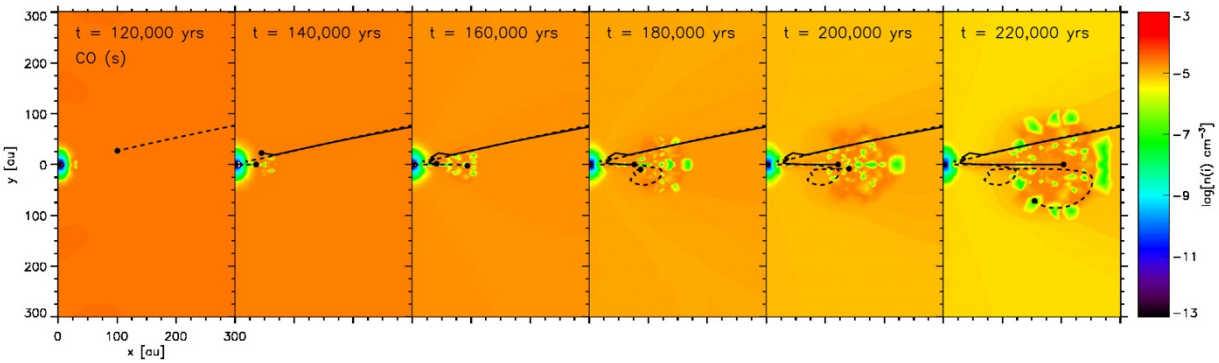

Figure 2 Abundance map of CO with respect to hydrogen. The solid-line corresponds to typical trajectory in the model. The dashed-line corresponds to a trajectory that has a near approach to the protostar, experiences high enoug h temperatures to desorb species from the grain, and results in a low-abundance pocket at the end of the model.

pressure drop and is recycled once again. However, in the case with this trajectory, this trajectory has a much lower abundance than the solid-line trajectory. This is denoted by the lower abundance color (green) in comparison to the solid-line trajectory's higher abundance color (orange), which represents over two orders of magnitude of abundance difference.

These two trajectories are just examples of two common paths for trajectories, and similar effects are seen in other trajectory paths. All trajectories that end in a low-abundance pocket experienced high enough temperatures as they approached the protostar to desorb CO off the grain. In addition to this low-abundance effect in place along different trajectory paths, it is also seen across species. Not only is CO subject to this low-abundance pattern, but so are other simple species and COMs.

Ice Column Densities

In order to compare to observations, we calculate the column density of each species along a line of sight. The lines of sight we consider are different inclinations, or viewing angles, into the protostar. For Class -I, every viewing angle yields the same column density as we assume spherical symmetry in the molecular cloud and there is no substantial effect on the column densities due to inclination until the model reaches Class I when the protostellar disk starts to form. Figure 3 plots the stage 1 (Class -I) and stage 2 (Classes 0 and I) absolute column density of water over time. In stage 2, there are twelve snapshot times we consider and each are denoted by a symbol. A vertical line that divides Class 0 from Class I is placed over the snapshot time in which the disk starts to form. The symbols correspond to a different inclination. Although inclinations from 0 to 90 were examined in increments of 15 degrees, Figure 3 shows only the inclinations of 90, 75, 60, and 0.

In addition to the absolute water ice column densities, the fractional column densities of various species with respect to water are plotted in Figure 4.

NIR38 and J110621, observed by McClure et al. (2023), are sightlines associated with the molecular cloud that is close in the sky to CHA MMS 1. Although these sightlines might note be directly related to a star-forming core, it is valuable to compare their ice abundances with our calculations during the pre-stellar core stage. Both sightlines were measured to have visual extinctions of 34 and 47 mag, respectively (Jimenez-Serra et al. (in prep)). In these measurements, the visual extinctions are based on absorption of the background stars' light through the entire cloud. To compare with our model, we therefore find the time which the model reaches an inner visual extinction equal to half the observed value, which is 17 mag and 23.5 mag for NIR38 and J110621, respectively. Therefore, the times that our inner most trajectory experiences visual extinctions of 17 mag and 23.5 mag are at times t=88,500 years and t=90,800 years in stage 1. These are the times where the data points are placed for NIR38 and J110621.

IRS4A was another source of study in the *Ice Age* program looking at the ice inventory in the class 0 source. IRS 4A has a visual extinction of 30 mag (Persi et al., 2001). The Rocha et al. (2024) JOYS+ program explored COM ice signatures in the low-mass class 0 IRAS 2A source. For the class

-I model data, we also compare to the range of column densities reported in Boogert et al. (2015). The Boogert et al. (2008) paper reports on column densities from the c2d spectroscopic survey of ices around low-mass YSO using the Spitzer Space Telescope. Of the sources included, we include HH 46 IRS, IRAS 17081-2721, and R Cr A IRS 5, all of which have conditions comparable to our models and have column densities reported for H_2O, CH_3OH, and HCOOH. The observational data is plotted in Figures 3 and 4 for comparisons to our modeled data. The Boogert et al. (2015) data is a range of column densities collected from various literature sources so the dotted green lines are the maximum and minimum of the range and the solid line is the median value. Otherwise, each observational data point/line includes its respective error bar, plotted as a dotted line. The values of the error bars can be found in their referenced articles. Note that some observational data has small error bars. Each source is indicated by a different color in the plots. Some sources only have an upper limit error bar so there is only one dashed line above the solid observational data line. The Boogert et al. (2015) data sometimes also only has one dotted line and that is an upper limit. Horizontal lines are used for observational data from Boogert et al. (2015), IRS 2A, IRS 4A, HH 46 IRS, IRAS 17081-2721, as their visual extinctions are not defined. Therefore, their column density value is stretched across all time to compare with the model.

Absolute Column Densities of H_2O

As shown in the plot on the left side of Figure 2, ice formation increases as time progresses and the molecular cloud collapses. As the molecular cloud collapses and ice abundance increases, the visual extinction increases towards the inner part of the cloud. For Class -I, NIR38 and J110621 more closely align with the model data at a later time in the molecular cloud collapse, where their visual extinction values match in the model. However, the model data does not overlap within the error bars of the observational data in Figure 3.

For Class 0, the absolute column density of H_2O matches the observational data for IRAS 2A earlier on in the model than HH 46 IRS. However, the model is within the bounds of all three observational comparisons. In Figure 2, the water ice falls as the center of the core warms up. In Class I, more ice is concentrated in the disk, so that the edge-on ice abundance grows as the disk grows. In the face-on case, ice column density falls as material is put into the disk and removed from the line of sight in the more polar directions.

When the model transitions to Class I, the inclination takes on a larger role in column density value. As mentioned above, the inclinations between 0 and 60 are not shown, due to their column densities closeness in value. After 60 degrees, the column density rises by at least an order of magnitude to 75 degrees, and then at least another order of magnitude to 90 degrees (edge-on). When referring back to Figure 1, the lines of sight for inclinations 60 to 90 go through the densest part of the disk, giving rise to a variance in column densities. The values from 0 to 60 degrees are outside the densest region of the disk and therefore, do vary greatly in their column density values.

Fractional Column Densities

In Figures 3 and 4 we present the column densities of species that have corresponding observational data from the literature. The sudden increase in absolute column density values in Figure 3, especially for those between 60-90 degrees, occurs when a disk starts to form. In Figure 4, the effect of growth of a disk is taken away because the values plotted are the fractional value of a specific species to water. Therefore, any deviation in column density due to inclination gives insight on the formation or destruction of that specific species.

In Figure 4 the fractional column density of CO with respect to water for the edge-on inclination of 90 degrees falls below the other inclinations' column densities. From Figure 2, we know that the H_2O column density is increasing over time, so the only way for the fractional abundance to drop is for CO column density to drop. When the disk starts to form at t=120,000 years, there is a drastic increase in density of H_2O near the protostar, particularly when viewing from an edge-on inclination. However, a disk with such close proximity to the protostar will be more heavily heated and water ice will not be able to retain CO. Therefore, the CO is lost at the early stages of disk formation. Once the disk grows outwards from the protostar, ices are able to regain CO on their surface. This is why there

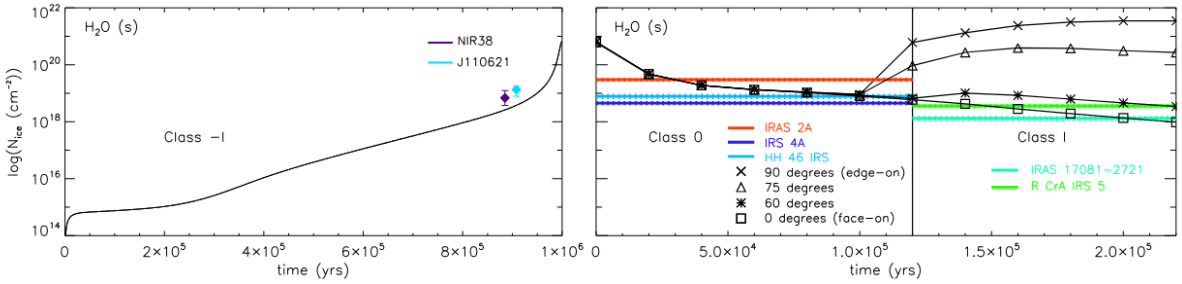

Figure 3 Stage 1 (Class -I) and stage 2 (Class 0 and I) ice column densities of water. Stage 1 column density of water is compared to ice observations towards two background stars, NIR38 and J110621. The observational values of the NIR38 and J110621 sources have been placed at the time in the model in which the visual extinction matches the source's calculated visual extinction. The calculated visual extinctions of NIR38 and J110621 are 34 mag and 47 mag, respectively (Jimenez-Serra et al. (in prep)). Stage 2 water column density is compared to observations of IRAS 2A, IRS4A, and HH46 IRS for Class 0 and IRAS 17081-2721 and CrA IRS 5 for Class I. The vertical black line separates Class 0 and Class I. In stage 2, there are twelve snapshot times represented by a symbol, with different symbols corresponding to various inclinations. Inclination of 90 degrees (edge-on) is marked by an X, 75 degrees is a triangle, 60 degrees is an asterick, and 0 degrees (face on) is a square. The vertical line aligns with the first time in the model where there is a divergence in column density due to inclination.

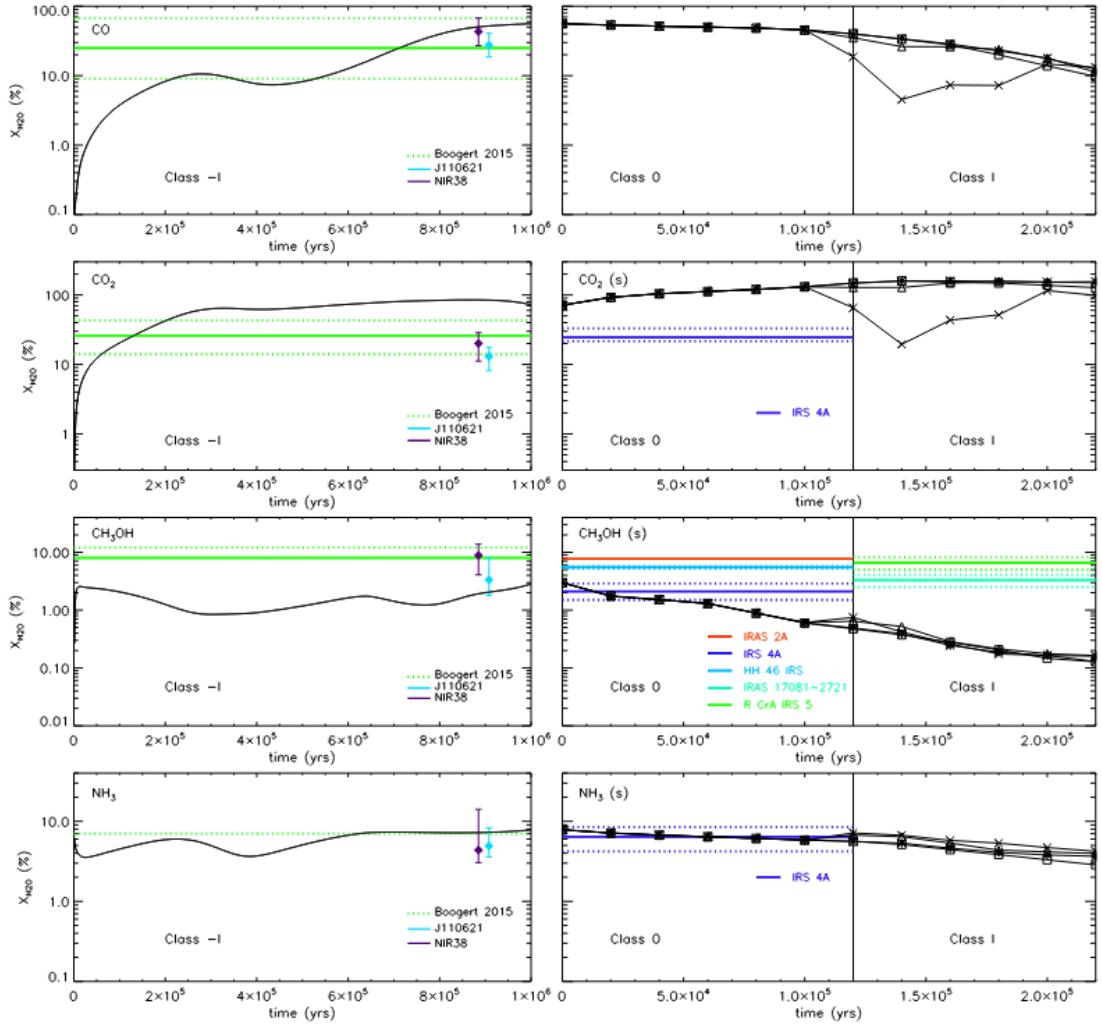

Figure 4 Stage 1 and 2 ice column densities with respect to water.

is an uptick in fractional column density at t=140,000 years. By the end of the model simulation, the CO is able to regain is original column density and converges with the other inclinations' column density values.

Another result to note is that the fractional column densities of CO, CH_3OH, and NH_3 decrease as the disk evolves. At the end of stage 1, when the cloud has collapsed, material on the outer edge of the cloud has a lower abundance than the inner part of the cloud. As the disk starts to form, the material from the outer part of the cloud will be added to the disk as the disk grows outward. When the material from the outer edge of the cloud joins the disk, these grains will have methanol at a lower abundance. Therefore, once these abundance values are now included in the column density calculation, the column density value will decrease over the remainder of Class I.

For CO column density values, there is only Class -I observational data to compare against. The model's column density values for all three sources falls within the range of the Boogert et al. (2015) data and fits within the error bars of the NIR38 data with the J110621 data not far off from the model.

For stage 1, the CH_3OH column density does fall within the error bar of J110621 and does not deviate more than an order of magnitude. For stage 2, the model intersects with the IRA 4A data during Class 0 but then continues to decrease through Class I and falls further away from observations of IRAS 17081 and R CrA IRS 5. In general, for the rest of the species, our model underproduces carbon-based species. If the initial carbon abundance is too low, subsequently, COMs will be underproduced as well.

However, our model's predictions for NH_3 align well with the Class -I, 0, and I observational data. Our model is within the error bars of both NIR38 and J110621 and under the upper limit from Boogert et al. (2015). For stage 2, the entirety of the model data for Class 0 falls within the error bars for IRS 4A.

Discussion

The goal of this project is to gain insight on the physical and chemical processes from the prestellar collapse to the formation of a protostellar disk. The multidimensional nature of the hydrodynamical chemical model allows insight to the spatial effects on simple and COM species throughout the cloud and disk. By running the model from Class -I through Class I, the model is able to trace the physical and chemical changes of ice species over time. The inclusion of inclination in the models allows for analysis of what column densities are obtained for various viewing angles. Analysis of the model's predictions with observational data gives insight as to how well our model behaves and what alterations may be needed.

Spatial Effects

As a 2D coupled hydrodynamical and chemical model, there are spatial effects on both the physics and chemistry. A notable physical, spatial effect relates the forces that act upon the trajectories and move them through the disk structure in Class I. In Figure 2, the effect of meridonial circulation is demonstrated, showing how a trajectory is pushed through the midplane and out and around the outer disk as it meets the sharp contrast in density structure. Therefore, this gives evidence that grain particles experience movement throughout the disk and the material is cycled.

Another physical-related effect on the spatial map of molecules is the temperature a trajectory experiences. Specific trajectories get close enough to the protostar before being pushed back through the midplane, resulting in higher temperatures enough to desorb certain molecules. The higher temperatures result in low-abundance pockets in the spatial abundance maps for COMs and simple, more volatile species. However, this effect occurred only for species that had a low enough binding energy that the high temperatures were enough to desorb them. Otherwise, molecules with higher binding energies were able to reaccrete onto the grain surface.

Alternatively, it can also be viewed that there is a pathway for the protection of species from the high temperatures and the species can survive at higher abundances in the outer disk. If the trajectories are able to not get too close to the protostar, and then are pushed through the midplane where temperatures are lower, they are able to be preserved. This is a potential explanation of how species are preserved into Class II and eventually incorporated into comets.

Temporal Effects

Our coupled hydrodynamical and chemical model is able to trace chemistry from the pre-stellar collapse through the formation of a disk. Figures 3 and 4 demonstrate that most of simple ice species and COMs are formed in the pre-stellar phase.

The species abundances stay consistent throughout Class 0. Once inclination angles start to have an effect on column densities (discussed below), we see variation in column densities as time progresses. In Figure 3, the column density of water increases over time as the disk grows. In any plots of the fractional column densities with respect to water in Figure 4 that have a dip in column density is due to trajectories with lower abundances from the outer envelope joining the disk.

Inclination Angle Effect

Another goal of this project is to examine the effect that the inclination angle, or viewing angle, has on the column densities of various species. In Figure 3, the effect of inclination does not affect the column density values until Class I when the protostellar disk starts to form. At the first snapshot time for Class I (denoted by the vertical line in Figure 3 there is a large deviation of the absolute column density of water of about 2 orders of magnitude for face-on inclination vs a edge on inclination. By the last snapshot time in Class I, the deviation between face-on and edge-on is about 3 orders of magnitude.

The largest jump in column density occurs for inclinations 60-90 degrees, with 90 degrees being the edge-on viewing angle. When comparing to Figure 1 these angles correspond to the densest part of the protostellar disk. Anything below 60 degrees has a small variation in column density compared to face-on, with the variation between 60 and 0 degrees being only about half of an order of magnitude. This result indicates that the column densities obtained from observations will be very sensitive to the inclination angle of that source and it should be expected that there will be variation of obtained column density values if observing sources that have inclination angles between 60-90 degrees.

Conclusions

We have presented a 2D coupled hydrodynamical and chemical model for a hot corino that traces the evolution of chemistry from the pre-stellar collapse through the formation of a disk. The radiation hydrodynamical model simulates the evolving density, temperature, and velocity structure of YSO Class -I into Class I. These values are fed into our chemical model, MAGICKAL, that are then run in post-processing to simulate the chemical evolution of each trajectory. MAGICKAL is a three-phase chemical kinetics model that simulates the gas, gas-grain, and mantle-ice chemistry. In this current project, we focus on the ice chemistry results and compare our results with recent JWST observations and other literature. Analysis of gas-phase chemistry is forthcoming in another paper.

The traced infall of trajectories and their movement through the disk has given better insight as to how the dynamics affects the chemistry. In the hydrodynamical results, we found evidence of meridonial circulation in the disk. This meridonial circulation allows the cycling of material throughout the protostellar disk and has a unique role in the spatial coverage of species. We discuss that trajectories that have a close approach to the forming protostar experience high enough temperatures that desorbs species from the grains surface. This close approach leaves these trajectories with lower ice abundances on the grain surface and as the motion of material throughout the disk pushes these trajectories out, they experience meridonial circulation and are pulled into low abundance pockets in the outer rim of the disk. This effect is amplified as time progresses in Class I.

In addition to the mechanism that cycles grains with low-abundances of select species, there is also movement of grains that are able to escape the harsh, higher temperatures near the protostar and are able to make their way through the motion of material within the disk with their high abundances of species still stable on the grain surface. In this case, the trajectories that keep stable abundances can be considered more pristine and may have a future role in conservation of COM material into comets.

This project also considered spatial maps for various species for all three YSO stages (Class -I, 0, and I). In the pre-stellar stage, the abundances are symmetrical around the cloud but vary with radius.

Column densities were calculated for Class -I, 0, and I and compared to observational JWST and Spitzer data. These comparisons showed agreement for some simple species such as CO, CH_3OH, and NH_3, but overall the models are underproducing.

A research question of interest in this project was whether the inclination has a role in whether a source is observed COM-rich or COM-poor. Our model shows that for inclinations between 60-90 degrees, the column density values can vary greatly. Below 60 degrees the column densities only varied less than an order of magnitude.

We summarize the main conclusions of this modeling study below:

i. Simple species and COMs are formed in the cold, pre-stellar stage, supporting the idea of early grain production of COMs.
ii. Meridonial circulation plays a role in the cycling of material throughout the disk.
iii. As material accretes onto star, trajectories that get near protostar but do not fall in, experience high temperatures that desorb ices and leave them with low-abundances for certain species.
iv. Trajectories with low-abundances from the close encounter to the protostar are moved along the midplane and to the outer rim of disk by the effect of meridonial circulation, creating "low-abundance" pockets.
v. Trajectories that do not get as near the protostar during accretion are able to survive with stable abundances, which is potentially a pathway that allows COMs to survive in the future incorporation into comets.
vi. Our models are generally underproducing grain chemistry, specifically for carbon-bearing species.
vii. Inclination angles between 60-90 degrees vary over three orders of magnitude and could have an impact on whether a source is observed to be COM-rich or COM-poor.
viii. Inclination angles below 60 degrees do not have a large variation in column density values as they are outside the main density structure of the disk.

Acknowledgements

This work was funded by the National Science Foundation through the Astronomy & Astrophysics program (grant number 2206516).

References:

Adams, F. C., Lada, C. J., & Shu, F. H. 1987, ApJ, 312, 788, doi: 10.1086/164924

Aikawa, Y., Wakelam, V., Garrod, R. T., & Herbst, E. 2008, The Astrophysical Journal, 674, 984, doi: 10.1086/524096

Aikawa, Y., Wakelam, V., Hersant, F., Garrod, R. T., & Herbst, E. 2012, The Astrophysical Journal, 760, 40, doi: 10.1088/0004-637X/760/1/40

Bacmann, A., Taquet, V., Faure, A., Kahane, C., & Ceccarelli, C. 2012, A&A, 541, doi: 10.1051/0004-6361/201219207

Belloche, A., Garrod, R. T., Müller, H. S. P., et al. 2019, A&A, 628, A10, doi: 10.1051/0004-6361/201935428

Belloche, A., Garrod, R. T., Zingsheim, O., Müller, H. S. P., & Menten, K. M. 2022, A&A, 662, A110, doi: 10.1051/0004-6361/202243575

Bhandare, Asmita, Commerçon, Benoît, Laibe, Guillaume, et al. 2024, A&A, 687, A158, doi: 10.1051/0004-6361/202449594

Bohlin, R. C., Savage, B. D., & Drake, J. F. 1978, ApJ, 224, 132, doi: 10.1086/156357

Boogert, A. A., Gerakines, P. A., & Whittet, D. C. 2015, Annual Review of Astronomy and Astrophysics, 53, 541–581, doi: 10.1146/annurev-astro-082214-122348

Boogert, A. C. A., Pontoppidan, K. M., Knez, C., et al. 2008, The Astrophysical Journal, 678, 985, doi: 10.1086/533425

Brinch, C., Jørgensen, J. K., & Hogerheijde, M. R. 2009, A&A, 502, 199, doi: 10.1051/0004-6361/200810831

Chuang, K.-J., Fedoseev, G., Ioppolo, S., van Dishoeck, E., & Linnartz, H. 2015, Monthly Notices of the Royal Astronomical Society, 455, 1702, doi: 10.1093/mnras/stv2288

Commerçon, B., Launhardt, R., Dullemond, C., & Henning, Th. 2012, A&A, 545, A98, doi: 10.1051/0004-6361/201118706

Coutens, A., Commerçon, B., & Wakelam, V. 2020, A&A, 643, A108, doi: 10.1051/0004-6361/202038437

Drozdovskaya, M. N., van Dishoeck, E. F., Rubin, M., Jørgensen, J. K., & Altwegg, K. 2019, Monthly Notices of the Royal Astronomical Society, 490, 50, doi: 10.1093/mnras/stz2430

Emerson, J. P., Harris, S., Jennings, R. E., et al. 1984, ApJL, 278, L49, doi: 10.1086/184220

Fedoseev, G., Chuang, K.-J., Ioppolo, S., et al. 2017, The Astrophysical Journal, 842, 52, doi: 10.3847/1538-4357/aa74dc

Fedoseev, G., Cuppen, H. M., Ioppolo, S., Lamberts, T., & Linnartz, H. 2015, Monthly Notices of the Royal Astronomical Society, 448, 1288, doi: 10.1093/mnras/stu2603

Furuya, K., Aikawa, Y., Tomida, K., et al. 2012, The Astrophysical Journal, 758, 86, doi: 10.1088/0004-637X/758/2/86

Garrod, R. T. 2013, ApJ, 765, 60, doi: 10.1088/0004-637X/765/1/60

Garrod, R. T., & Herbst, E. 2006, A&A, 457, 927, doi: 10.1051/0004-6361:20065560

Garrod, R. T., Jin, M., Matis, K. A., et al. 2022, The Astrophysical Journal Supplement Series, 259, 1, doi: 10.3847/1538-4365/ac313127

Garrod, R. T., Wakelam, V., & Herbst, E. 2007, A&A, 467, 1103, doi: 10.1051/0004-6361:20066704

Henderson, B. L., & Gudipati, M. S. 2015, The Astrophysical Journal, 800, 66, doi: 10.1088/0004-637X/800/1/66

Herbst, E., & van Dishoeck, E. F. 2009, Annual Review of Astronomy and Astrophysics, 47, 427, doi: 10.1146/annurev-astro-082708-101654

Hincelin, U., Commerçon, B., Wakelam, V., et al. 2016, The Astrophysical Journal, 822, 12, doi: 10.3847/0004-637X/822/1/12

Hocuk, S., Szűcs, L., Caselli, P., et al. 2017, A&A, 604, A58, doi: 10.1051/0004-6361/201629944

Hosokawa, T., & Omukai, K. 2009, The Astrophysical Journal, 691, 823, doi: 10.1088/0004-637X/691/1/823

Ioppolo, S., Kaňuchová, Z., James, R. L., et al. 2020, A&A, 641, A154, doi: 10.1051/0004-6361/201935477

Jensen, S. S., Jørgensen, J. K., Furuya, K., Haugbølle, T., & Aikawa, Y. 2021, A&A, 649, A66, doi: 10.1051/0004-6361/202040196

Jiménez-Serra, I., Vasyunin, A. I., Caselli, P., et al. 2016, The Astrophysical Journal Letters, 830, L6, doi: 10.3847/2041-8205/830/1/L6

Jiménez-Serra, I., Rodríguez-Almeida, Lucas F., Martín-Pintado, Jesús, et al. 2022, A&A, 663, A181, doi: 10.1051/0004-6361/202142699

Jin, M., & Garrod, R. T. 2020, The Astrophysical Journal Supplement Series, 249, 26, doi: 10.3847/1538-4365/ab9ec8

Jin, M., Lam, K. H., McClure, M. K., et al. 2022, ApJ, 935, 133, doi: 10.3847/1538-4357/ac8006

Jørgensen, J. K., Belloche, A., & Garrod, R. T. 2020, Annual Review of Astronomy and Astrophysics, 58, 727, doi: 10.1146/annurev-astro-032620-021927

Jørgensen, J. K., Favre, C., Bisschop, S. E., et al. 2012, The Astrophysical Journal, 757, L4, doi: 10.1088/2041-8205/757/1/l4

Jørgensen, J. K., Bourke, T. L., Myers, P. C., et al. 2005, The Astrophysical Journal, 632, 973, doi: 10.1086/433181

Lam, K. H. 2022, PhD Dissertation, University of Virginia, doi: https://doi.org/10.18130/x2qv-6j63

Marcelino, N., Cernicharo, J., Agúndez, M., et al. 2007, The Astrophysical Journal, 665, L127, doi: 10.1086/521398

Masunaga, H., & Inutsuka, S.-i. 2000, The Astrophysical Journal, 531, 350, doi: 10.1086/308439

Masunaga, H., Miyama, S. M., & ichiro Inutsuka, S. 1998, The Astrophysical Journal, 495, 346, doi: 10.1086/305281

McClure, M. K., Rocha, W. R. M., Pontoppidan, K. M., et al. 2023, Nature Astronomy, 7, 431–443, doi: 10.1038/s41550-022-01875-w

Megías, A., Jiménez-Serra, I., Martín-Pintado, J., et al. 2022, Monthly Notices of the Royal Astronomical Society, 519, 1601, doi: 10.1093/mnras/stac3449

Nazari, P., Tabone, B., Rosotti, G. P., et al. 2022, A&A, 663, A58, doi: 10.1051/0004-6361/202142777

Persi, P., Marenzi, A. R., Gómez, M., & Olofsson, G. 2001, A&A, 376, 907, doi: 10.1051/0004-6361:20010962

Rocha, W. R. M., & Pilling, S. 2020, The Astrophysical Journal, 896, 27, doi: 10.3847/1538-4357/ab91bd

Rocha, W. R. M., van Dishoeck, E. F., Ressler, M. E., et al. 2024, A&A, 683, A124, doi: 10.1051/0004-6361/202348427

Rocha, W. R. M., McClure, M. K., Sturm, J. A., et al. 2025, A&A, 693, A288, doi: 10.1051/0004-6361/202451505

Shope, B. M., El-Abd, S. J., Brogan, C. L., et al. 2024, The Astrophysical Journal, 972, 146, doi: 10.3847/1538-4357/ad5d5f

Stone, J. M., Gardiner, T. A., Teuben, P., Hawley, J. F., & Simon, J. B. 2008, The Astrophysical Journal Supplement Series, 178, 137, doi: 10.1086/588755

Stone, J. M., Tomida, K., White, C. J., & Felker, K. G. 2020, The Astrophysical Journal Supplement Series, 249, 4, doi: 10.3847/1538-4365/ab929b

Stutz, A. M., Rubin, M., Werner, M. W., et al. 2008, The Astrophysical Journal, 687, 389, doi: 10.1086/591789

Tu, Y., Li, Z.-Y., & Lam, K. H. 2022, Monthly Notices of the Royal Astronomical Society, 515, 4780, doi: 10.1093/mnras/stac2030

Vazzano, M. M., Fernández-López, M., Plunkett, A., et al. 2021, A&A, 648, A41, doi: 10.1051/0004-6361/202039228

Visser, R., Bergin, Edwin A., & Jørgensen, Jes K. 2015, A&A, 577, A102, doi: 10.1051/0004-6361/201425365

Visser, R., Doty, S. D., & van Dishoeck, E. F. 2011, A&A, 534, A132, doi: 10.1051/0004-6361/201117249

Visser, R., van Dishoeck, E. F., Doty, S. D., & Dullemond, C. P. 2009, A&A, 495, 881, doi: 10.1051/0004-6361/200810846

Yang, Y.-L., Green, J. D., Pontoppidan, K. M., et al. 2022, The Astrophysical Journal Letters, 941, L13, doi: 10.3847/2041-8213/aca289

Öberg, K. I., Bottinelli, S., Jørgensen, J. K., & van Dishoeck, E. F. 2010, The Astrophysical Journal, 716, 825, doi: 10.1088/0004-637X/716/1/825